

Research Article www.acsami.org

Selective Reduction of Multivariate Metal—Organic Frameworks for Advanced Electrocatalytic Cathodes in High Areal Capacity and Long-Life Lithium—Sulfur Batteries

Mahmoud M. Kaid, Mohammad K. Shehab, Hong Fang, Awad I. Ahmed, Sohier A. El-Hakam, Amr Awad Ibrahim, Puru Jena, and Hani M. El-Kaderi*



Cite This: ACS Appl. Mater. Interfaces 2024, 16, 2283-2295



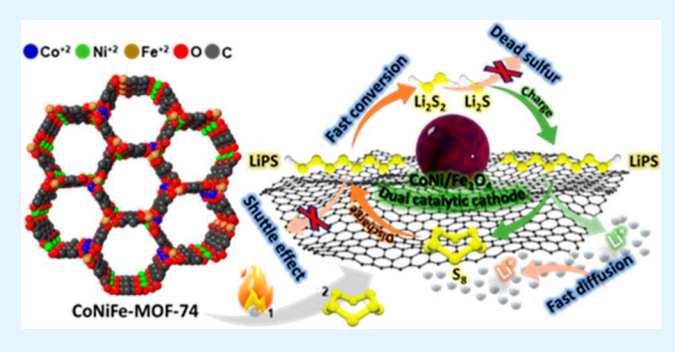
ACCESS I

III Metrics & More

Article Recommendations

Supporting Information

ABSTRACT: Lithium-sulfur batteries hold great promise as nextgeneration high-energy-density batteries. However, their performance has been limited by the low cycling stability and sulfur utilization. Herein, we demonstrate that a selective reduction of the multivariate metal-organic framework, MTV-MOF-74 (Co, Ni, Fe), transforms the framework into a porous carbon decorated with bimetallic CoNi alloy and Fe₃O₄ nanoparticles capable of entrapping soluble lithium polysulfides while synergistically facilitating their rapid conversion into Li₂S. Electrochemical studies on coin cells containing 89 wt % sulfur loading revealed a reversible capacity of 1439.8 mA h g⁻¹ at 0.05 C and prolonged cycling stability for 1000 cycles at 1 C/1060.2 mA h g⁻¹ with a decay rate



of 0.018% per cycle. At a high areal sulfur loading of 6.9 mg cm⁻² and lean electrolyte/sulfur ratio (4.5 μ L:1.0 mg), the battery based on the 89S@CoNiFe₃O₄/PC cathode provides a high areal capacity of 6.7 mA h cm⁻². The battery exhibits an outstanding power density of 849 W kg⁻¹ at 5 C and delivers a specific energy of 216 W h kg⁻¹ at 2 C, corresponding to a specific power of 433 W kg⁻¹. Density functional theory shows that the observed results are due to the strong interaction between the CoNi alloy and Fe₃O₄, facilitated by charge transfer between the polysulfides and the substrate.

KEYWORDS: lithium-sulfur batteries, metal-organic frameworks, electrocatalytic cathodes, lithium polysulfide shuttling, high areal capacity, high energy density

INTRODUCTION

There has been an increasing demand for cost-effective highenergy-density batteries to store energy from intermittent sources such as solar and wind to mitigate the adverse effects of fossil fuels (limited supply and environmental impact manifested by global warming). Due to the multielectron redox reactions of the sulfur cathode, lithium-sulfur batteries (LSBs) hold great promise among next-generation battery technologies, given their low cost, sulfur abundance, and high energy density compared to lithium-ion batteries (LIBs). 1-5 At theoretical volumetric and gravimetric capacities of 2800 W h L⁻¹ and 2567 W h Kg⁻¹, respectively, LSBs have the desired merits to address the market demand for hybrid and electric vehicles with tangible societal and environmental impacts.^o Even though intense research activities have been directed at advancing LSBs, their widespread use has been impeded by their low stability and short cycling life. It has been accepted that such shortcomings arise due to soluble lithium polysulfide (LiPS) dissolution into the electrolytes known as the "shuttle effect," low sulfur utilization, and the insulating nature of sulfur and Li₂S. During battery discharge, the sluggish reaction

kinetics hinder rapid sulfur conversion into the desired Li₂S at the cathode, promoting LiPS leaching out of the cathode and migrating through the separator to react at the lithium anode surface, causing anode passivation and hence degrading battery capacity and stability upon cycling.8,9

To address the stability issue of the LSBs, several strategies have been developed including modifying the sulfur host to immobilize sulfur species and enhance their redox kinetics. For example, integrating polar sites in the sulfur host and modifying catalytic species have been the most effective approach. These studies have focused on various transition-metal dichalcogenides and pnictides. ^{10–12} For instance, metal nitrides, metal phosphides, metal borides, and metal sulfides have been proven to be effective mediators with efficient

October 16, 2023 Received: Revised: December 12, 2023 Accepted: December 12, 2023 Published: January 2, 2024





Scheme 1. Schematic Representation of CoNiFe-MOF-74 Synthesis and Its Thermal Transformation into the S@CoNiFe₃O₄/ PC Cathode, Followed by Coin Cell Assembly and Typical GCD Profile



catalytic activity and high adsorption capability for LiPS confinement. In searching for cost-effective and efficient catalysts, metal oxides have also been explored to advance cathode stability and performance due to their unique band structure and ability to provide rich adsorption sites for anchoring LiPS. 13-15 However, metal oxides exhibit limited catalytic activity and low conductivity, which limit their effectiveness in advancing LSBs. 16-18 Metal-based materials can catalytically promote the conversion of long-chain LiPS into short-chain LiPS and then to Li2S by adsorbing and oxidizing long-chain LiPS, thus, restraining the shuttle effect. Among the used metals, Co, Ni, and Fe supported on carbons have attracted increased attention in battery-type storage because of their lower intercalation potential. 19-21 However, the weak metal-carbon interactions in such systems limit their catalytic activity.²² Furthermore, bimetallic alloying has been explored to optimize the electronic structure of mono metals and to alter the weak interaction between metals and carbons to enhance their catalytic nature. 22,23

The many prerequisites of sulfur hosts, i.e., high sulfur loading, electrical conductivity, high LiPS affinity, fast lithiumion diffusion, and rapid redox kinetics, can be addressed using a bottom-up approach using metal-organic frameworks (MOFs). MOFs are highly designable porous materials constructed from organic linkers and metal ions. With a judicious selection of metal ions and organic linkers, physicochemical properties can be fine-tuned to address a broad range of applications, such as gas storage and separation, catalysis, sensing, and electrochemical energy storage. 24-26 In particular, MOFs and their derivatives were recently applied in the energy storage field.^{27,28} Moreover, the calcination of MOFs provides metals and metal oxide embedded in conductive porous carbon, maximizing the possibility of electronic conductivity and allowing for easy access to lithium ions.²⁹ Pristine MOFs used as electrodes in batteries have been mainly restricted by their stability issues, low capacity, poor conductivity, and weak adhesion to the substrate. On the other hand, functional MOF derivatives such as metal sulfides, metal phosphide, metal oxides, and nanometals embedded in porous

carbons are generally more efficient for rechargeable batteries.30-32 The unique structural features of MOFs and their ability to coordinate different metal ions in their secondary building units as in the case of multivariate-MOFs (MTV-MOFs), makes MOFs uniquely suited for advancing the design and performance of electrocatalytic electrodes. This top-down approach enables rapid cathode fabrication and eliminates several challenges encountered with traditional methods like wet chemical methods of coprecipitation and impregnation or gas phase processes, including chemical vapor deposition and atomic layer deposition that suffer from metal nanoparticle agglomeration or the need for advanced fabrication tools. 34,35 To this end, we envisioned that thermolysis of MTV-MOFs of selected metal composition under controlled reaction conditions could lead to superior sulfur cathodes that combine a high LiPS anchoring ability and rapid redox kinetics.

Despite significant advances, most reported studies used coin-cell configurations under uncontrolled Li anode conditions, excessive electrolytes, and low sulfur mass loadings. The high-energy advantage is significantly offset by the use of a large proportion of inactive materials, thus limiting their practicality. Accordingly, the highest priority for future perspectives on developing high energy-density LSBs and designing practical LSB technologies are (1) design of smart cathodic electrocatalyst hosts with interconnected and highly porous materials, good conductivity, high adsorption ability to simultaneously achieve diffusion, adsorption, and fast catalytic conversion of polysulfides, (2) reducing electrolyte to sulfur ratio $(R_{\rm E/S})$ and increasing areal cathode capacity $(m_{\rm sl})$ are critical to attaining ultrahigh energy density of 800-1000 W h kg-1 in future LSBs, and (3) increasing both the specific capacity based on sulfur (C_{sulfur}) and V_{cathode} can considerably improve the power and energy densities.

To realize high-energy-density LSBs, all of these critical parameters must be carefully considered. Herein, we demonstrate that controlled pyrolysis of MTV-MOF-74 (Co, Ni, and Fe) affords a unique catalytic sulfur host composed of CoNi-Fe₃O₄ nanoparticles supported on porous carbon

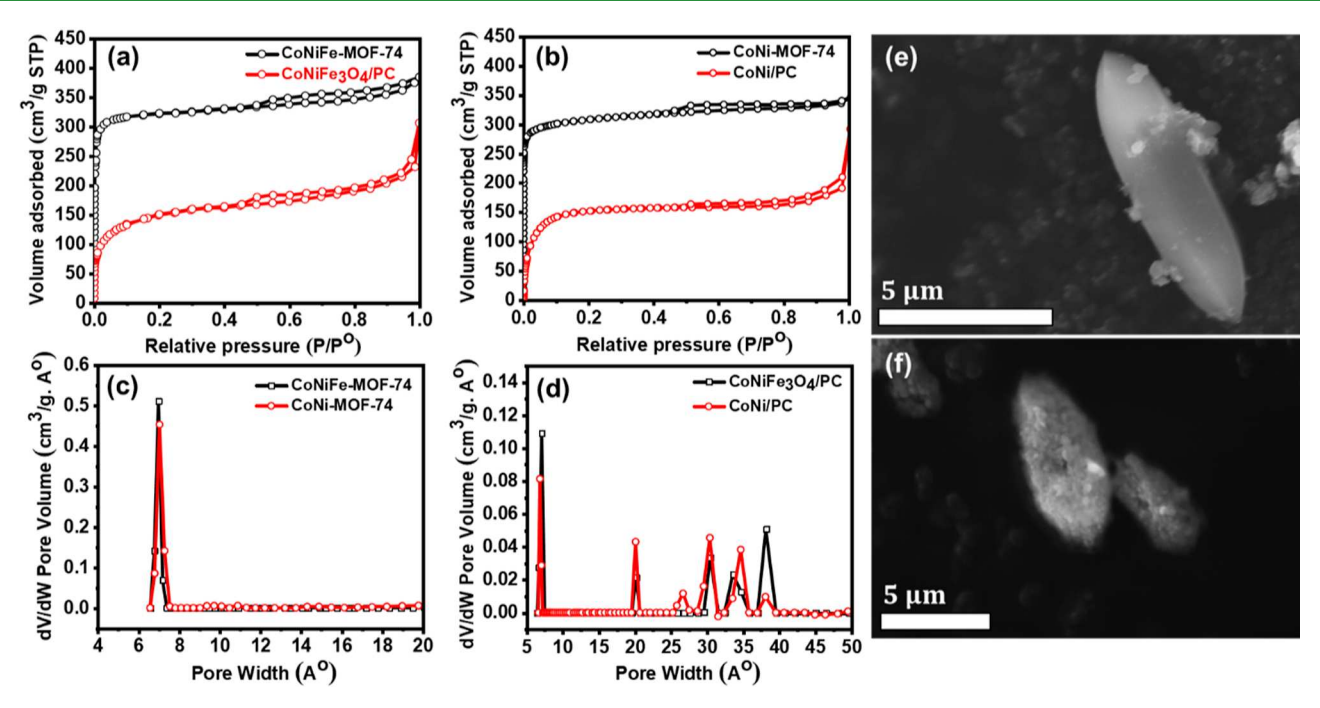


Figure 1. (a,b) N_2 adsorption—desorption isotherm and (c,d) pore size distribution of the prepared samples. SEM of (e) CoNiFe-MOF-74 and (f) CoNiFe₃O₄/PC.

(CoNiFe₃O₄/PC), which exhibits superior cathodic performance due to the synergistic effect of CoNiFe₃O₄. The CoNiFe₃O₄/PC electrocatalyst combines the strong adsorption capacity of Fe₃O₄ toward LiPS and the redox activity of the CoNi alloy. Batteries derived from S@CoNiFe₃O₄/PC exhibit high capacity, high-rate capability, and superior long-term cycling stability even at high sulfur loading and lean electrolyte content, highlighting the effect of the MOFs selection and pyrolysis conditions on battery stability and performance. Future perspectives on developing high energy-density LSBs are also described considering all critical parameters for designing practical LSB technologies.

■ RESULTS AND DISCUSSION

Because of their promising potential in LSBs, bimetallic CoNi alloys and Fe₃O₄ nanoparticles were targeted to alleviate the shuttle effect and enhance the sluggish redox kinetics at the cathode. Therefore, CoNiFe-MOF-74 with metal contents of Co = 13.8, Ni = 6.5, and Fe = 7.0 wt % was targeted. A one-pot solvothermal reaction of dioxidoterephthalate with the divalent metals in DMF/ethanol/water afforded porous phase-pure MOF-74 according to XRD, porosity, and SEM studies. 37,38 Thermolysis conditions of CoNiFe-MOF-74 were carefully selected to assess the impact of the temperature and reduction atmosphere on the physical and chemical properties of the resultant metal-doped carbon and to determine how such properties dictate battery stability and performance, especially at high sulfur loading and lean electrolyte content. Our thermolysis strategies depended on the fact that the metals used in synthesizing CoNiFe-MOF-74 decompose in the order of Ni, Co, and then Fe under thermal treatment control.³⁷ The resultant porous carbon also benefits from the porous channels of the pristine MOF, which gives rise to facile lithium-ion diffusion during battery cycling and enables high sulfur loading.^{33,35} Two pyrolysis approaches were employed to rationalize the role of the metals in enhancing the battery

performance. First, CoNiFe-MOF-74 was pyrolyzed at 400 °C for 1 h (ramping rate = 2 °C min⁻¹) under N₂/H₂ (5% hydrogen) flow. This process transforms the MOF into a CoNi alloy and Fe₃O₄ supported on porous carbon (Scheme 1). The total decomposition of MOF at 600 °C under N₂/H₂ seems facile and afford CoNiFe/PC, but it is not optimized for Li–S batteries due to the destruction of the well-defined channel/pore structures of MOF and the dramatic decrease in the surface area (Figure S1a).

The nitrogen adsorption-desorption isotherms of CoNiFe-MOF-74, CoNi-MOF-74, CoNiFe₃O₄/PC, and CoNi/PC samples were acquired to verify the porosity of the MOFdriven CoNiFe₃O₄/PC, as shown in Figure 1a,b. The Brunauer-Emmett-Teller (BET) specific surface area of CoNiFe-MOF-74 and CoNi-MOF-74 was calculated in the P/P_0 range of 0.05-0.30 (Figure S1b) to be 1282 and 1229 m²/g, respectively, and classified as a typical type I isotherm. The specific surface area of the pyrolyzed samples maintained about 69% of the original surface area of the pristine MOFs. Additionally, the corresponding pore size distribution measured by nonlocal density functional theory (NLDFT) indicates that most pores of the parent MOFs were microporous (Figure 1c). In contrast, the pore size range extended to the mesoporous range after carbonization (Figure 1d), which is beneficial for high sulfur loading and overcoming volume fluctuations. 22,33,35 The TGA-MS analysis indicates the thermal decomposition of the CoNiFe-MOF-74 into CoNiFe₃O₄/PC at ~400 °C (Figure S2a). Because the trimetallic Co, Ni, and Fe-MOF-74 can be deoxygenated in the order of Ni, Co, and then Fe, a thermal treatment control was considered to obtain CoNi alloy and Fe₃O₄ embedded in residual porous carbon, a signature of this decomposition was observed in TGA-MS.³⁷ Sulfur loading was accomplished by using the melt-diffusion approach. The sulfur content and thermal stability of the S@CoNiFe₃O₄/PC composite were investigated using TGA-MS analysis under the N2 atmosphere (Figure S2b). TGA-MS analysis of S@CoNiFe₃O₄/PC

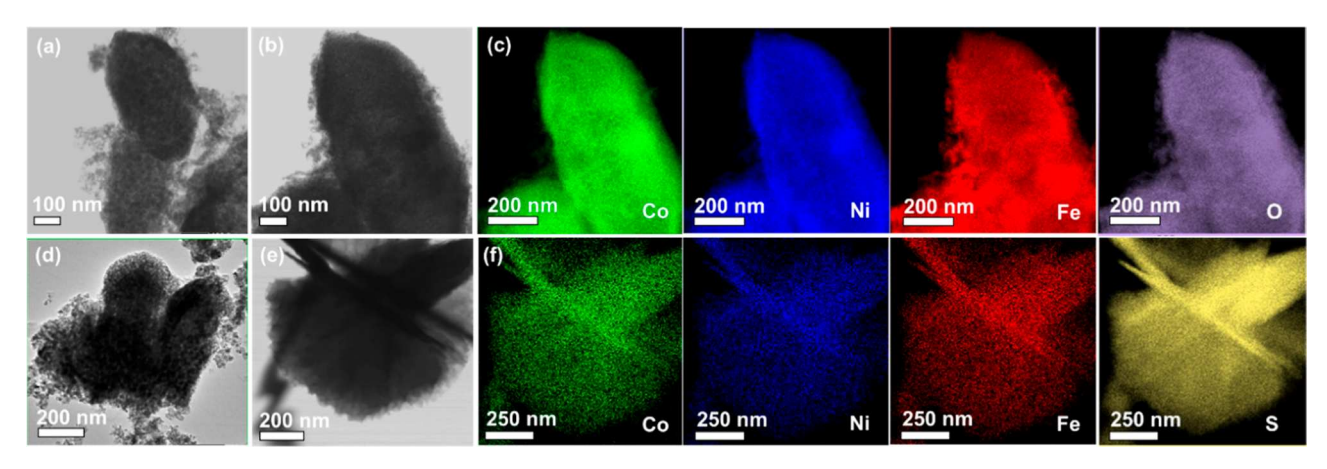


Figure 2. TEM images and the corresponding EDS mapping of (a-c) CoNiFe₃O₄/PC and (d-f) S@CoNiFe₃O₄/PC.

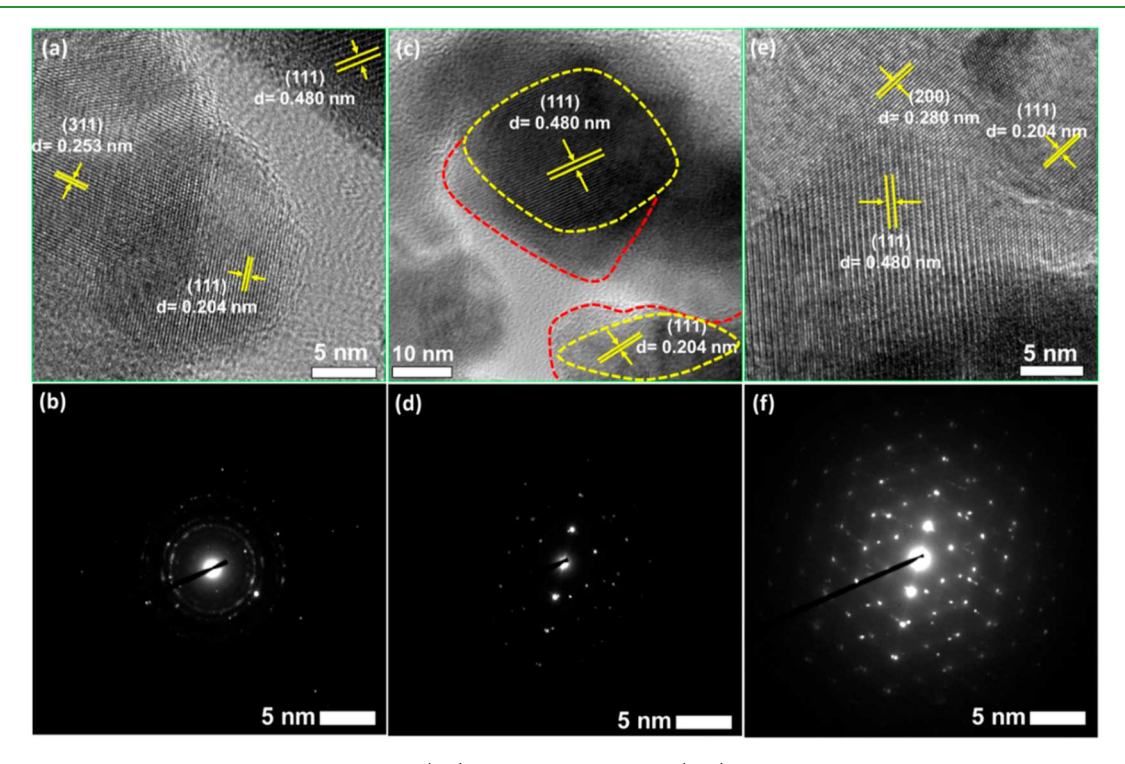


Figure 3. High-resolution TEM and SAED patterns of (a,b) CoNiFe $_3$ O $_4$ /PC and (c-f) S@CoNiFe $_3$ O $_4$ /PC. The yellow dotted line indicates CoNiFe $_3$ O $_4$ nanoparticles, and the red dotted line indicates the formation of NiCo $_2$ S $_4$ shell after sulfurization of CoNiFe $_3$ O $_4$ /PC.

revealed a sulfur content of 89 wt % in agreement with the targeted loading (90 wt %) and was also confirmed by EDS analysis (88 wt %). It is worth noting that high sulfur content is very desirable to attain high areal energy density in LSBs but often results in low sulfur utilization in the absence of catalysts.²³

The synthetic process of CoNiFe₃O₄/PC was targeted with an atom ratio of Co/Ni (Fe) ~ 2:1 to obtain CoNi alloy with the highest fcc-phase strength based on the Co-Ni-Fe phase diagram. The Co-Ni phase diagram indicates that the hardness of CoNi alloys increases as the cobalt content increases. Thus, increasing the cobalt content in the crystal is beneficial for the stability of the structure. ICP-OES and EDS were used to analyze the proportion of Co, Ni, and Fe and the average metal weight percent of bare and carbonized CoNiFe-MOF-74 (Table S1). The elemental analysis data reveal high metal content in the carbonized MOF; Co: 32.45, Ni: 15.05, and Fe: 16.27 wt % with an atom ratio of Co/Ni

(Fe) \sim 2:1. The X-ray powder diffraction peaks obtained for CoNiFe₃O₄/PC and CoNi/PC confirmed that CoNi alloy is present as fcc crystal (Figure S3). The two strong peaks at 2θ = 44.43 and 51.91° can be indexed to the (111) and (200) planes of face-centered cubic (fcc) phase of CoNi, respectively, (JCPDS no. 15-0806 for fcc Co, JCPDS no. 04-0850 for fcc Ni). The characteristics peaks of Fe₃O₄ are located at 2θ = 18.4, 30.30, 35.53, 43.02, 53.59, and 57.53°, which correspond to the (111), (220), (311), (400), (422), and (511) crystal planes of Fe₃O₄ (JCPDS no. 65-3107). 44,45 To investigate the role of Fe₃O₄ in cathode function, CoNi-MOF-74 with similar Co and Ni contents, 13.8 and 6.5 wt %, respectively, was also synthesized and annealed under identical conditions as stated earlier to afford the expected characteristic peaks for the fcc CoNi alloy supported on porous carbon (Figure S3b). To validate the effectiveness of CoNi alloy and Fe₃O₄ in LSBs, the S@CoNiFe₃O₄/PC cathode was prepared for battery studies. The XRD pattern of S@CoNiFe₃O₄/PC reveals the distinct

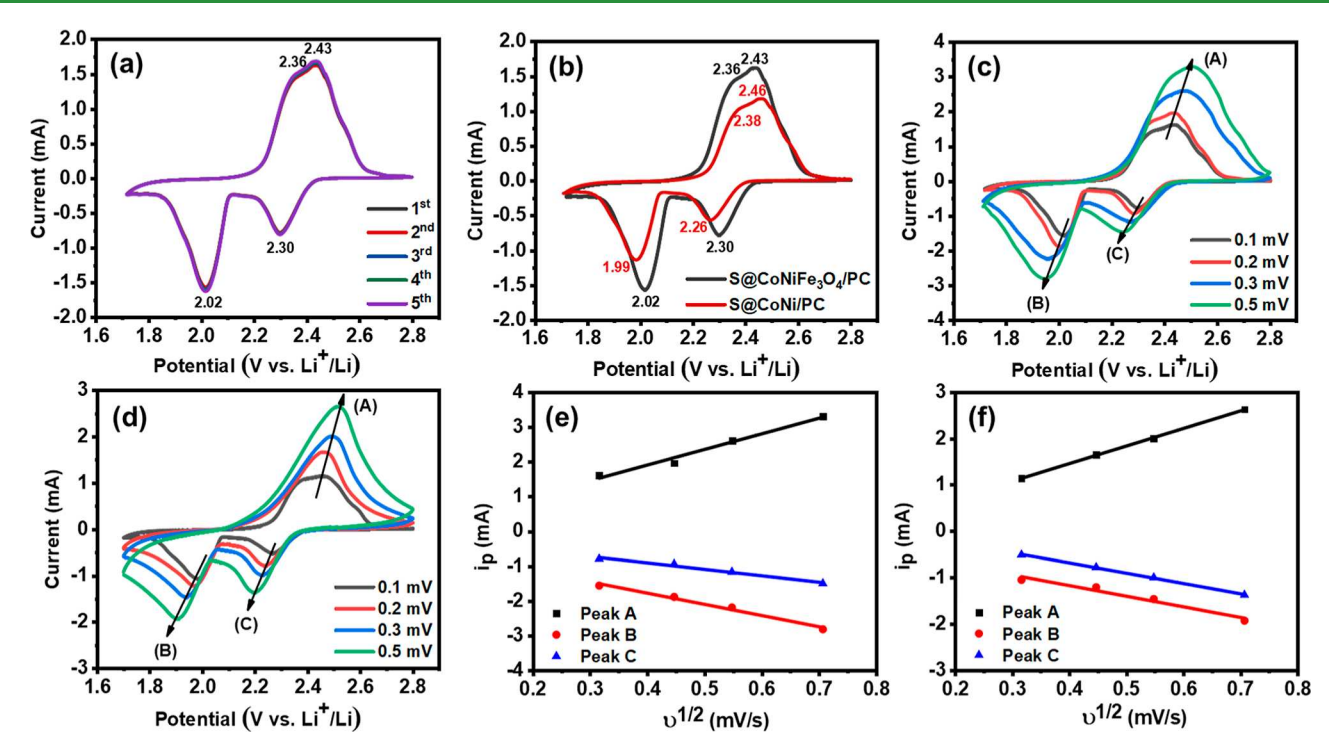


Figure 4. (a) CV curves of LSBs using the S@CoNiFe₃O₄/PC cathode at 0.1 mV s⁻¹. (b) First cycle CV of LSBs using S@CoNiFe₃O₄/PC and S@CoNi/PC cathodes. CV profiles at different scan rates were obtained using (c) S@CoNiFe₃O₄/PC and (d) S@CoNi/PC cathodes. The corresponding i_p – $\nu^{1/2}$ scatters and linear fitting of the anodic and cathodic peaks in the CV curves of (e) S@CoNi-Fe₃O₄/PC and (f) S@CoNi-/PC.

characteristic peaks of sulfur (PDF # 08-0247), as shown in Figure S3. ²³ Importantly, all of the peaks can be indexed to sulfur, CoNi alloy, NiCo₂S₄, and Fe₃O₄. Surface oxidation of CoNi alloy during sulfur loading has been reported and depends on the composition of CoNi alloys. ^{46–48} The superimposition of the CoNi alloy phase and NiCo₂S₄ phase (JCPDS no. 20-0782) indicates the formation of a thin layer of CoNi–sulfide on the surface of the CoNi alloy. ⁴⁹ This sulfide layer was further verified by the TEM and HR-TEM images of S@CoNiFe₃O₄/PC.

SEM images of CoNiFe-MOF-74 and CoNiFe₃O₄/PC indicated that the pyrolyzed MOF at 400 °C maintains its crystal shape, except the surface becomes rough due to ultrafine nanoparticles formation from partial MOF decomposition (Figure 1e,f). Such a structure is further confirmed by TEM, as shown in Figures 2 and S4. TEM images in Figure S4 reveal that the CoNi alloy is enriched as a skin shell over the Fe₃O₄ surface, which is first deposited in the core. Moreover, the formation of the NiCo₂S₄ shell after sulfurization of CoNiFe₃O₄/PC is clearly observed in Figure S4e and verified by HR-TEM. The porous structure of the carbonized MOF was also observed in the TEM images (Figure S4f) and confirmed the BET analysis. The dense packing of the Co, Ni, and Fe₃O₄ clusters becomes evident through the energydispersive X-ray spectroscopy (EDS) studies, and no agglomerates were found despite the high cluster density (Figure 2). The elemental mapping of each element (Co, Ni, Fe, O, and S) shows that all expected metals are spread out within the carbon matrix and verifies the well-defined CoNiFe₃O₄/PC structure with a high density of Co, Ni, Fe, and O elements, as shown in Figure 2c. It should be noted that sulfur is uniformly distributed and effectively accommodated in the mesopores of CoNiFe₃O₄/PC even with a high sulfur

content of 89 wt %, as shown in Figure 2f. Moreover, the quantitative analysis obtained from the EDS spectra agreed with the targeted loading and is consistent with the ICP results, as shown in Figure S5 and Table S1.

HR-TEM analysis with selected area electron diffraction (SAED) was carried out to investigate the structural and morphological features of CoNiFe₃O₄/PC and S@CoNiFe₃O₄/PC (Figure 3). The magnified HR-TEM image of the MOF-driven CoNiFe₃O₄/PC clearly shows the formation of lattice fringes corresponding to the interplanar spaces of 0.204, 0.253, and 0.480 nm and in agreement with the facet of CoNi (111), Fe_3O_4 (311), and Fe_3O_4 (111), respectively (Figure 3a). 50-52 The same result was obtained from the SAED pattern (Figure 3b), which confirmed that the MOFdriven CoNiFe₃O₄/PC is highly crystalline. The absence of fringes in the carbon layer of CoNiFe₃O₄/PC supports the formation of amorphous carbon. These results are consistent with the XRD results, where the peaks of CoNi and Fe₃O₄ can be detected obviously; however, no diffraction peaks related to carbon can be observed. Moreover, HR-TEM confirmed the sulfurization of CoNiFe₃O₄/PC has uniform crystallinity for each nanoparticle with a new d-spacing of 0.280 nm observed to the (200) planes of NiCo₂S₄ (Figure 3c,e).⁵³ The distances between the lattice fringes in S@CoNiFe₃O₄/PC were calculated at various regions indicated as 1, 2, and 3, as shown in Figure S6. NiCo₂S₄ was observed to be present in the interface of the CoNi alloy and Fe₃O₄ nanoparticles after sulfurization of CoNiFe₃O₄/PC. Furthermore, the interplanar distances of (111) planes of Fe₃O₄ and CoNi alloys were found to be 0.480 and 0.204 nm, respectively. Along with the abovementioned lattice fringes, the SAED pattern images of CoNiFe₃O₄/PC (Figure 3b) and S@CoNiFe₃O₄/PC (Figure 3d,f) were found to contain clear bright spots, which suggested

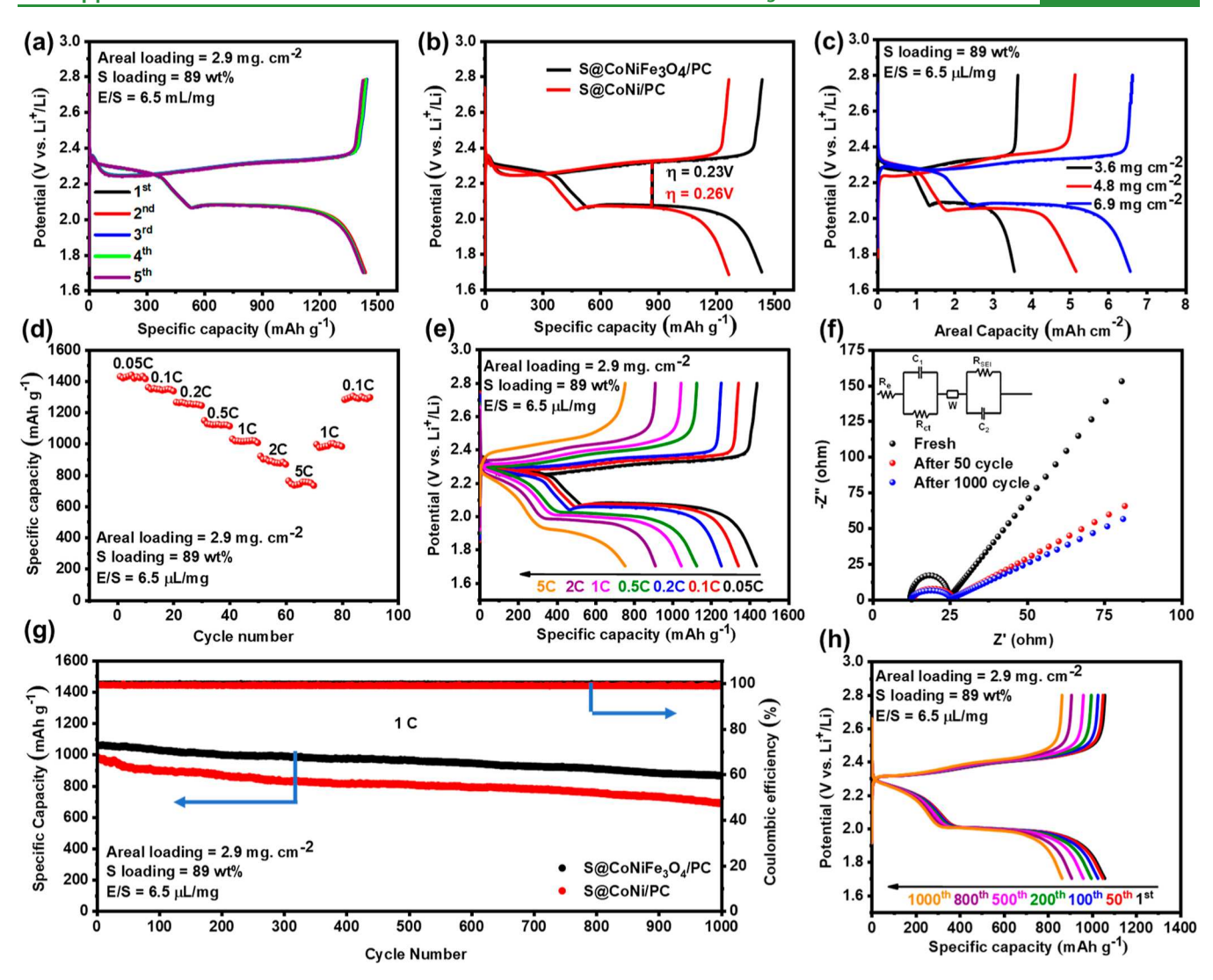


Figure 5. (a) Charge—discharge profiles of a Li—S battery using a S@CoNiFe $_3$ O $_4$ /PC cathode at 0.05 C. (b) First GCD of the S@CoNiFe $_3$ O $_4$ /PC and S@CoNi/PC cathodes at 0.05 C. (c) Areal capacity of the S@CoNiFe $_3$ O $_4$ /PC cathodes at 0.1 C with various areal sulfur loadings. (d,e) GCD of S@CoNiFe $_3$ O $_4$ /PC at varied current rates (0.05–5 C). (f) EIS data of standard LSBs with S@CoNiFe $_3$ O $_4$ /PC cathode. (g,h) Long-term cycling stability of S@CoNiFe $_3$ O $_4$ /PC and S@CoNi/PC electrodes at a 1.0 C rate for 1000 cycles.

the high crystallinity of the prepared electrocatalysts. This also confirms that both cobalt and nickel nanoparticles are present in monophase with a highly crystalline structure.

The X-ray photoelectron spectroscopy (XPS) was used to determine the chemical composition of CoNiFe-MOF-74 and CoNiFe₃O₄/PC (Figures S7 and S8). High-resolution XPS C 1s spectra of CoNiFe-MOF-74 and CoNiFe₃O₄/PC show similar spectra, which can be split into four subpeaks (Figure S7). However, the peaks related to the oxygen-containing functional groups are much less intense, indicating the partial reduction of CoNiFe₃O₄/PC after pyrolysis of CoNiFe-MOF-74 at 400 °C. Such reduction increases the aromatic character, turning the MOF-driven CoNiFe₃O₄/PC into a more conductive material. 54,55 The bonding decomposition during partial pyrolysis of CoNiFe-MOF-74 at 400 °C was also examined by XPS, implying the complete decomposition of Co and Ni nodes in CoNiFe-MOF-74 to form metal nanoparticles (Figure S8). For Co 2p, the peak at a binding energy of 782.4 eV attributed from Co-O (Co²⁺) contribution is shifted to lower binding energy (778.7 eV), indicating that Co-O bonds in CoNiFe-MOF-74 are completely decomposed and reduced

to metallic cobalt (Co⁰).⁵⁶ The XPS spectra of Ni 2p showed similar structural changes. The peak for Ni²⁺ at 856.8 eV evolved into a new spin-orbit splitting peak at 852.6 eV, characteristic of Ni⁰ after pyrolysis of CoNiFe-MOF-74 under N₂/H₂.⁵⁷ Lastly, as can be seen from the high-resolution XPS of Fe $2p_{3/2}$ (Figure S8), the peak from Fe-O (Fe³⁺) contribution remained as the major peak, indicating most of the iron in MOF-74 remained trivalent and was not decomposed after pyrolysis CoNiFe-MOF-74 at 400 °C.58 It is intriguing to note that the ionic valence state of metals is detected in CoNiFe₃O₄/PC for Fe 2p, which is otherwise missing in the XPS Co 2p and Ni 2P. In contrast, the zero valence state of metals is detected for Co 2p and Ni 2P and missed in the XPS Fe 2p, indicating that only Co-O and Ni-O bonds are decomposed during pyrolysis of CoNiFe-MOF-74 at 400 °C.

To evaluate the synergistic effect of CoNi and Fe₃O₄, cyclic voltammetry (CV) curves of S@CoNiFe₃O₄/PC and S@CoNi/PC-based cells were acquired for 5 cycles in a potential window of 1.7-2.8 V at a scan rate of 0.1 mV s⁻¹ (Figures 4 and S9). The results show that the S@CoNiFe₃O₄/PC cathode

has good electrochemical reversibility and stable cycling performance (Figure 4a). Compared with the S@CoNi/PC cathode, the oxidation peak of the S@CoNiFe₃O₄/PC cathode has a slight change to lower potential, and the reduction peaks shift to higher potentials (Figure 4b). The S@CoNiFe₃O₄/PC cathode has a sharper peak shape and higher peak current density than the S@CoNi/PC cathode, indicating a faster LiPS conversion ability and lower polarization of the S@ CoNiFe₃O₄/PC cathode. This phenomenon shows the enhanced polysulfide redox kinetics by CoNiFe₃O₄/PC nanoparticles. In the CV curve of S@CoNiFe3O4/PC, the first two sharp cathodic peaks at 2.30 and 2.02 V were attributed to reducing S_8 to Li_2S_x (x = 4-8) and further conversion to short-chain Li₂S₂ or Li₂S. 59,60 Furthermore, the CV curves of the five cycles show overlapping after the first cycle, indicating good reversibility of the electrochemical process. The above results reflect the role of Fe₃O₄ in adsorbing the polysulfides during the discharge process and their rapid conversion to Li₂S by CoNi. The results also support the rapid conversion of Li₂S into S₈ during the reverse oxidation process.

CV tests were also collected at various scan rates from 0.1 to 0.5 mV s⁻¹ to further evaluate the diffusion characteristics of Li⁺ ions (Figure 4c,d). The peak current data were analyzed using the Randles–Sevick eq 1 to determine the contribution of S@CoNiFe₃O₄/PC and S@CoNi/PC to the redox kinetics of the cell, and the results are shown in Figure 4e,f. 61,62

$$I_{\rm p} = 0.4463nFAC(nF\nu D/RT)^{1/2}$$
 (1)

where i_p is the peak current (mA), ν represents the rated scan speed (mV s⁻¹) employed in the CV test, T is the absolute temperature (298.0 K), R is the ideal gas constant (8.314 J $\text{mol}^{-1} \text{ K}^{-1}$), and D is the lithium-ion diffusion coefficient (cm² s^{-1}). F, n, A, and C represent the Faraday constant (96485 C mol⁻¹), number of electron transfer (2 for LSBs), electrode surface area (2.54 cm²), and lithium-ion concentration parameters (mol cm⁻³), respectively. Choosing the cathodic and anodic peak currents (A–C) in the CV curves to map $v^{1/2}$ is shown in Figure 4e,f. The results show that all reduction and oxidation current peaks are linearly related to the square root of the scanning rate, and the peak current increases by increasing the scanning rate. The slope of S@CoNiFe₃O₄/PC is higher than that of S@CoNi/PC, indicating that the Li+ diffusion coefficient is enhanced by the polar sites due to Fe₃O₄. This proves that due to its LiPS adsorption and catalytic effects, S@CoNiFe₃O₄/PC can accelerate the redox kinetics of LSBs.

The galvanostatic charge/discharge (GCD) profiles of S@ CoNiFe₃O₄/PC at a current rate of 0.05 C were also obtained in the range of 1.7–2.8 V (Figure 5a). A representative discharge process with two plateaus near 2.32 and 2.06 V corresponds to the conversion from S₈ to long-chain polysulfides (Li₂S₈, Li₂S₆, and Li₂S₄) and the further reduction to insoluble short-chain Li₂S₂ or Li₂S, coinciding with the CV curve results. To verify the superiority of S@CoNiFe₃O₄/PC, the first GCD curves of the S@CoNiFe₃O₄/PC and S@CoNi/PC cathodes at 0.05 C are compared in Figure 5b. The discharge plateaus of the S@CoNiFe₃O₄/PC cathode are flatter and more extended with higher capacity (1439.8 mA h g⁻¹) than those of S@CoNi/PC (1229.8 mA h g⁻¹) and lower polarization ($\eta = 0.23$ V), elucidating the improved kinetic characteristics of the S@CoNiFe₃O₄/PC cathode. The initial

discharge capacity of $S@CoNiFe_3O_4/PC$ at 0.05 C (1439.8 mA h g^{-1}) is higher than that of S@CoNi/PC (1229.8 mA h g^{-1}), most likely due to the enhanced LiPS adsorption by Fe_3O_4 . The impact of sulfur loading on accessible capacity was studied; $S@CoNiFe_3O_4/PC$ cathodes with different sulfur loadings of 71, 80, and 89 wt % were prepared and tested, as shown in Figure S10. The highest capacity was observed for the cathode with the highest sulfur loading (89 wt %, 1439.8 mA h g^{-1} at 0.05 C), which indicates excellent sulfur utilization.

To further understand the cathode's thickness influence on the electrochemical properties of the batteries, several cathodes with different weight loadings between 3.5 and 7.0 mg cm⁻² were fabricated and tested at a current rate of 0.1 C (Figure 5c). Even at a high areal sulfur loading of 6.9 mg cm $^{-2}$, the cell with S@CoNiFe₃O₄/PC cathode possessed excellent electrochemical performance with an areal capacity of 6.7 mA h cm⁻². Furthermore, the galvanostatic discharge-charge was applied at varied current rates (0.05-5.0 C) to evaluate the rate capability of the S@CoNi-Fe₃O₄/PC cell, as shown in Figure 5d,e. At different rates, the S@CoNiFe₃O₄/PC electrode with sulfur loading of 89 wt % displayed good charge exchange kinetics during lithiation/delithiation processes. The S@ CoNiFe₃O₄/PC cathode exhibited a tapering capacity from 1439.8 mA h g⁻¹ at 0.05 C to 1343.2, 1255.3, 1127.6, 1047.6, 912.4, and 755.8 mA h g⁻¹ at 0.1, 0.2, 0.5, 1, 2, and 5 C, respectively. Notably, a reversible capacity of 1286.9 mA h g⁻¹ was recovered when the current rate was reduced from 5.0 to 0.1 C, demonstrating the high reversibility and low attenuation ability of S@CoNiFe₃O₄/PC. According to the above results, the bimetallic alloy/metal oxide combination strategy is vital for enhancing the cathode stability against the shuttle effect in LSBs. These results reflect the significantly improved electrochemical performance of the S@CoNiFe₃O₄/PC cathode, which can be attributed to the enhanced conductivity, adsorption ability, and catalytic conversion effect of CoNiFe₃O₄/PC.

Electrochemical impedance spectroscopy (EIS) studies of S@CoNiFe₃O₄/PC and S@CoNi/PC were performed before cycling and after 50 and 1000 cycles of GCD measurements. As shown in Figures 5f and S11, the results signified a smaller charge transfer resistance value (12.3 Ω) for S@CoNiFe₃O₄/ PC compared to the S@CoNi/PC cathode (32.9 Ω). The Nyquist diagram consists of a long slash and a semicircle in the low and high-frequency regions, respectively. The intercept of the real part Z' in the high-frequency region corresponds to the total Ohm resistance (R_e) , including the resistance due to the circuit, the electrode, and the electrolyte. The semicircle in the high-intermediate frequency region represents the charge transfer resistance (R_{ct}) , which is indicated by the charge transfer process at the electrolyte-electrode interface. Moreover, lithium-ion diffusion is attributed to the short oblique line corresponding to the Warburg impedance (W) in the lowfrequency region.⁶³ Based on the equivalent circuit in the inset of Figures 5f and S11, the values of Re and Rct for S@ CoNiFe₃O₄/PC cathode are 12.6 and 12.3 Ω , which are both smaller than 17.3 and 32.9 Ω for S@CoNi/PC cathode, respectively. Therefore, the S@CoNiFe₃O₄/PC cathode can lower the charge transfer impedance to a certain extent and has preferable conductivity and a faster charge transfer rate compared to those of the S@CoNi/PC cathode. The lithium-ion diffusion coefficients for S@CoNiFe₃O₄/PC and S@CoNi/PC before cycling were calculated based on eqs \$1

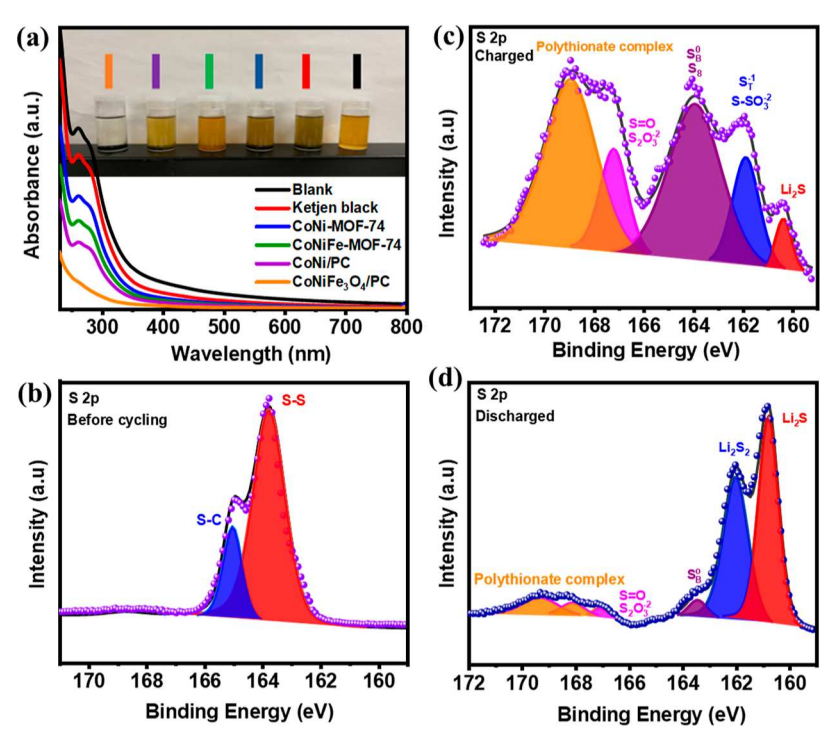


Figure 6. (a) UV-vis spectrum and optical picture to illustrate the adsorption of Li₂S₆. High-resolution XPS of the S@CoNiFe₃O₄/PC cathode (b) before cycling, (c) fully charged after 100 cycles GCD, and (d) fully discharged after 100 cycles GCD.

and S2, and Figure S12 and were found to be 1.71×10^{-10} and 7.95×10^{-11} cm² s⁻¹, respectively. Thus, the S@CoNi/PC cathode exhibits a lower lithium-ion diffusivity compared with S@CoNiFe₃O₄/PC. The superiority of S@CoNiFe₃O₄/PC mainly arises from the strong LiPS adsorption, Li₂S rapid conversion reaction, faster ion/electron transportation, and Li⁺ diffusion.

The cycling durability of LSBs assembled from S@ CoNiFe₃O₄/PC and S@CoNi/PC cathodes are displayed in Figure 5g,h. The S@CoNiFe₃O₄/PC electrode with 89 wt % sulfur loading exhibited a significantly enhanced cycling stability at 1.0 C with higher capacity retention and Coulombic efficiency than S@CoNi/PC after 1000 cycles. The cathode with an areal sulfur loading of 2.9 mg cm⁻² reveals a surprising initial discharge specific capacity of 1060.2 mA h g⁻¹ at 1 C and retained a discharge specific capacity of 864.9 mA h g⁻¹ in the 1000th cycle with a retention rate of 81.6% and a fade rate of 0.018% per cycle. In comparison, the S@CoNi/PC cathode shows a discharge capacity of 983.1 mA h g⁻¹, suggesting lower utilization of active materials and retained 689.2 mA h g⁻¹ after 1000 cycles with a retention rate of 71.0%. The electrochemical performance of LSB cells with the S@CoNiFe₃O₄/ PC cathode compared with previously reported metal and metal oxides-based host materials (Table S2) indicates that S@ CoNiFe₃O₄/PC exhibits superior rate capability and cycling stability. These results confirm that the unique compassion of the S@CoNiFe₃O₄/PC cathode is central to extending the cycling life of LSBs.

To evaluate $S@CoNiFe_3O_4/PC$ in addressing the shuttle effect of LiPS, we examined the LiPS—CoNiFe₃O₄ interactions using a solution of Li₂S₆ (10 mM) prepared from the reaction between Li₂S and S in a 1:5 molar ratio in a solvent mixture of DME and DIO (Figure 6a). Adding the yellow solution of Li₂S₆ to CoNiFe₃O₄/PC resulted in discoloration of the solution, as shown by the inset photograph in Figure 6a. In

comparison, the addition of Li_2S_6 to the pristine MOF-74, Ketjen black, and CoNi/PC did not lead to a noticeable color change, which supports the effective role of Fe₃O₄ in anchoring soluble LiPS. The peak around 260 nm in the UV—vis spectra is related to the S_6^{2-} species. ^{14,19} Compared with the blank (Li₂S₆ solution), the peak intensity of the solution after CoNiFe₃O₄/PC adsorption was significantly decreased and much lower than those with MOF-74, Ketjen black, and CoNi/PC. This suggests a fast Li₂S₆ adsorption by Fe₃O₄ in the CoNiFe₃O₄/PC composite, which is very important for mitigating the shuttle effect of soluble polysulfides.

The LiPS-CoNiFe₃O₄ interaction was also examined by XPS analysis of S 2p, as shown in Figure 6b,c. High-resolution XPS of S 2p before cycling the battery (Figure 6b) reveals two $S 2p_{3/2}$ peaks at 165.1 eV (S-C) and 163.8 eV (S-S).⁶⁴ Upon galvanostatic charge-discharge (GCD) for 100 cycles, the extracted S@CoNiFe3O4/PC cathode of a fully charged battery showed a strong S 2p contribution peak at 163.9 eV, which matches the peak observed for S₈ before cycling and indicates the conversion of Li₂S into elemental sulfur after charging the battery to 2.8 mV. Additional sulfur environments (Figure 6c) showed peaks at 167.2 and 168.9 eV and corresponded to the formation of thiosulfate and polythionate complexes, respectively, due to Li₂S_x/Fe₃O₄ surface interaction. These peaks are in precise accord with S=O or the central sulfur in thiosulfate $([SSO_3]^{-2})$, whereas its peripheral sulfur is fitted at 161.9 eV. 14,15 The terminal (S_T^{-1}) sulfur atoms at 160.4 eV are contributing to the residual Li₂S. This suggests a good interaction between Fe₃O₄ and polysulfides and fast catalytic conversion by CoNi NPs. XPS analysis conducted on S@CoNiFe₃O₄/PC which was extracted from a completely discharged battery after 100 cycles is shown in Figure 6d. The weak S 2p_{3/2} long-chain polysulfide contribution at 163.5 eV is consistent with the complete conversion into shorter-chain polysulfides. Moreover, the

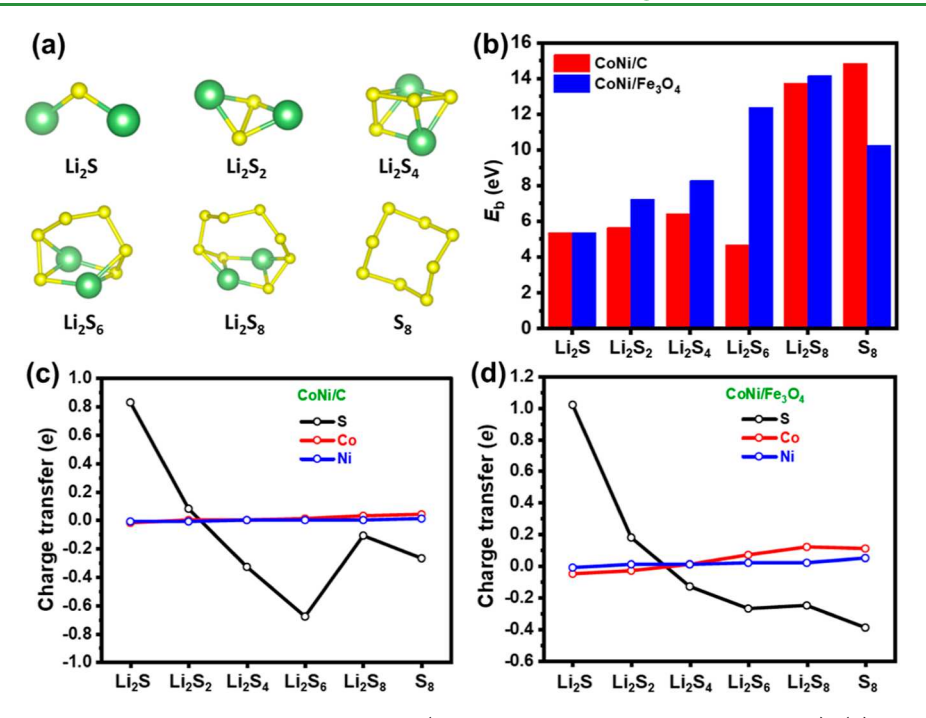


Figure 7. (a) Optimized polysulfide configurations in the gas phase (S is represented in yellow and Li in green). (b) Calculated binding energies (according to eq 2) of the polysulfides interacting with the interface models. (c,d) Calculated charge transfer of S to the polysulfides, as well as Co and Ni in the CoNi alloy.

thiosulfate and polythionate complex peaks between 167.1 and 169.3 eV have vanished after discharge to 1.7 mV, which is also accompanied by the transformation of long-chain to shorterchain polysulfides. The thiosulfate and polythionate complex peaks are precisely the same as observed in the S 2p spectrum of fully charged batteries, except with much lower intensities. The formation of shorter-chain polysulfides accompanies the difference in relative intensities ascribed to the consumption of longer-chain polysulfides. According to the results presented above, the redox reaction between Li₂S_x and Fe₃O₄ forms thiosulfates on the surface of the cathode. The insoluble S₂O₃⁻² anchored long-chain polysulfides, and the CoNi NPs catalyze the catenation reaction by insertion in the S-S single bond to create shorter-chain polysulfide species and polythionate complex via internal disproportionation reaction as shown in Figure S13. 15,65

Results based on DFT calculations are consistent with those from the experiment. The cyclic S_8 polysulfide configurations (Li₂S, Li₂S₂, Li₂S₄, Li₂S₆, Li₂S₈, and S₈) in the gas phase have been optimized (Figure 7a) and their adsorption on the CoNi/C interface and the CoNi/Fe₃O₄ interface systems are studied (see Theoretical Method in the Supporting Information). The strength of interaction between the polysulfide and the interface structure is measured by the binding energy (E_b) defined in eq 2

$$E_{\rm b} = E_{\rm tot} - E_{\rm int} - E_{\rm PS} \tag{2}$$

where $E_{\rm tot}$ $E_{\rm int}$ and $E_{\rm PS}$ are the ground-state energies of the polysulfide adsorbed interface, the interface structure, and the gas phase polysulfide cluster, respectively. The interaction of the polysulfides with the interfaces is extraordinarily strong, especially with the CoNi/Fe₃O₄ interface. The calculated binding energies are much greater than that (\sim 4.4 eV) of the best single-atom catalyst anchored on N-doped carbon matrices, as shown by the calculated binding energy in Figure 7b. Upon interacting with the CoNi/C interface, Li–S

bonds in the small polysulfides, including Li₂S and Li₂S₂, are elongated by ~0.3 Å. Li₂S₄ and Li₂S₆ are restructured (compared to their gas-phase configurations) upon interaction with the interface. Li₂S₈ and S₈ are disintegrated due to the strong interaction between S and the interface, as shown in Figure S14. Compared to the CoNi/C interface, the CoNi/ Fe₃O₄ provides even stronger catalytic power, avoiding the formation of any large polysulfides (Li₂S₆ onward) in the first place, as shown in Figure S15. The Li-S bonds in the small polysulfides Li₂S and Li₂S₂ are elongated as much as ~0.9 Å when they interact with the CoNi/Fe₃O₄ interface. The binding energies between the polysulfides and CoNi/Fe₃O₄ are all greater than 5.3 eV, as shown in Figure 7b. All of the above results are summarized in Table S3. The strong interaction between the polysulfides and the interface structures is due to the large charge transfer between S and the substrates, as shown in Figure 7c,d. For the small polysulfides Li₂S and Li₂S₂, the charge transfer is from S to the substrate. From Li₂S₄ onward, the charge transfer is from the substrate to S in the polysulfide. Since charge transfer at the CoNi alloy is negligibly small, as shown in Figure 7c,d, most of the charge transfer is between the polysulfide and the substrate of carbon or Fe₃O₄. The reason that the CoNi/Fe₃O₄ interface can provide extraordinary catalytical power is due to the strong interaction between CoNi alloy and Fe₃O₄, facilitating charge transfer between the polysulfides and the substrate (Fe₃O₄). The calculated binding energy between CoNi and Fe₃O₄ is 1.72 eV/CoNi, which is much higher than the 0.14 eV/CoNi between CoNi and carbon. The strong interaction between CoNi and Fe₃O₄ is due to the formation of a Ni-O bond at the interface. It is found that, in the optimized CoNi/Fe₃O₄ interface model, there is a charge transfer of 0.1e per Ni from Ni to Fe₃O₄ and a charge transfer of 0.02e per Co from Fe₃O₄ to Co, making CoNi become more polarized.

Energy density calculation was investigated based on critical parameters, including sulfur mass ratio, electrolyte/sulfur ratio,

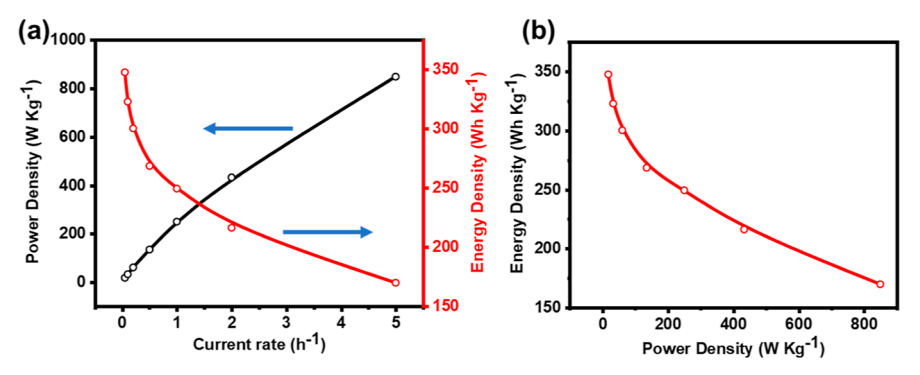


Figure 8. (a) Power density and energy density of the 89S@CoNiFe₃O₄/PC battery at different current rates of 0.05 to 5 C. (b) Ragone plot.

areal sulfur mass loading, and negative-to-positive electrode material ratio according to the recent method developed by Cui et al.³⁶ Considering all critical parameters for designing practical LSBs technologies, two descriptors (R_{energy} and R_{weight}) were used to analyze the energy- and mass-level compromises on the LSB cell energy density. Besides the anode and cathode materials, the coin cell consists of a current collector, an electrolyte, a separator, and an external case for shielding the battery core from the air. These battery components are electrochemically inactive materials except for sulfur loaded in the cathode (m_{sI}) and active Li in the anode. The mass of the cathode $(m_{cathode})$ includes a sulfur host, conducting material, and binder agent used to stabilize the cathode and boost sulfur utilization. Moreover, an excess of Li is also needed beyond the active Li to prolong the cycle life during battery operation. The descriptor R_{weight} depicts the total mass percentage of both $m_{\rm sI}$ and active Li, as shown in eq S3. In addition to the mass-level compromise (inactive-massrelated issues), we considered the energy loss due to voltage polarizations and incomplete reactions (energy-level compromise). In an ideally completed electrochemical reaction, the reaction enthalpy (2 equiv of Li and 1 equiv of sulfur to form Li₂S) is converted to electric energy at an average output voltage of 2.2 V (based on the difference in their electrode potentials) and affords 1675 mA h g⁻¹ (the theoretical specific capacity based on the mass of sulfur). However, in real LSBs, converting lithium and sulfur into Li2S can hardly be completed because some sulfur species (such as Li₂S₈, Li₂S₆, and Li₂S₄) could leach into electrolytes and are not part of the subsequent electrochemical reactions that lead to Li₂S. Moreover, some sulfur materials (such as Li₂S₂) formed during discharge remain in intermediate states rather than completely converted to Li₂S. Comparing the specific capacity of sulfur (C_{sulfur}) with its theoretical capacity reflects this degree of reaction completion. On the other hand, voltage polarizations occur during operation, such as concentration, ohmic, and activation, decreasing the average output voltage $(V_{average})$ and producing a proportional loss of output energy. Accordingly, the energy utilization ratio (R_{energy}) of active materials is calculated by combining energy loss from both the polarization-induced result (V_{average} divided by the theoretical voltage) and the incomplete electrochemical reactions (C_{sulfur} divided by the theoretical capacity), as shown in eq S4. The gravimetric energy density of LSBs was calculated based on both the mass- and energy-level compromises (Rweight and $R_{\rm energy}$), as shown in eq S5.

Power density and energy density measurements were carried out to determine the electrocatalytic effect of

CoNiFe₃O₄/PC on battery performance. Combining both high power density and high energy density is necessary for practical applications. The 89S@CoNiFe₃O₄/PC-based battery attains a remarkable energy density of 567 W h kg⁻¹ at 0.05 C (Figure 8a), higher than those reported for best-performing metallic- and metal oxides-based electrodes for LSBs. $^{67-70}$ In terms of power density (eq S6), 89S@CoNiFe₃O₄/PC exhibits an outstanding power density of 849 W kg⁻¹ at 5 C and delivers a specific energy of 216 W h kg⁻¹ within 6.1 min at 2 C, which corresponds to a specific power of 433 W kg⁻¹ (Figure 8b). These results reflect the significantly improved electrochemical performance of S@CoNiFe₃O₄/PC. Our cathode design provides both high $R_{\rm weight}$ and $R_{\rm energy}$, leading to increased energy densities, as shown in Figure 8.

Finally, the LBS based on the S@CoNiFe₃O₄/PC cathode showed good storage stability at room temperature. Upon GCD measurements of a fresh assembled S@CoNiFe₃O₄/PC battery for 5 cycles, the battery was rested and tested after 3 months. The fully charged S@CoNiFe₃O₄/PC battery showed self-discharge at 2.8 eV before being stabilized at 2.34 eV. After the first cycle, the GCD pattern of the stored battery matches the one observed for the fresh battery with no significant decrease in the specific capacity after being stored for 3 months, as shown in Figure S16. The results indicate that the S@CoNiFe₃O₄/PC cathode has a limited reduction against Li/ Li⁺ over time and good stability, ensuring suitability for longterm storage. These achievements mostly rely on the smart design of CoNiFe₃O₄ with interconnected and highly porous carbon materials as cathodic electrocatalyst hosts to simultaneously achieve the diffusion, adsorption, and fast catalytic conversion of polysulfides.

CONCLUSIONS

To conclude, we have demonstrated that thermolysis and selective reduction of the multivariate metal—organic framework, MTV-MOF-74 (Co, Ni, and Fe), affords highly porous carbon with an impeded bimetallic CoNi alloy and Fe₃O₄ nanoparticles for entrapping soluble lithium polysulfides while synergistically facilitating their rapid conversion into Li₂S. This work provides an effective strategy for exploring MOFs-derived materials for high-areal capacity and long-life Li–S batteries. The superior performance of S@CoNiFe₃O₄/PC is ascribed to the efficient adsorption of lithium polysulfide species by Fe₃O₄ and the catalytic effect of CoNi alloy toward polysulfides conversion augmented by high sulfur loading and electrical conductivity of the porous carbon host. The S@CoNiFe₃O₄/PC cathode exhibits impressive electrochemical performances, including a high initial discharge specific capacity of 1439.8 mA

h g⁻¹ at 0.05 C, which remains significantly high even at a high C rate (755.8 mA h g^{-1} at 5 C). Battery stability was remarkable, and after 1000 cycles, a capacity of 864.9 mA h g⁻¹ at 1 C with a prominent capacity retention rate of 81.6% and a low decay rate of 0.018% per cycle was observed. Impressively, the LSB-based S@CoNiFe₃O₄/PC demonstrated an ultrahigh power density of 849 W kg⁻¹ at 5 C and delivered a specific energy of 216 W h kg⁻¹ at 2 C, which corresponds to a specific power of 433 W kg⁻¹. Density functional theory-based calculations show that the underlying physical principles guiding the experimental results are due to the strong interaction between the CoNi alloy and Fe₃O₄, facilitating charge transfer between the polysulfides and the substrate (Fe₃O₄). This work highlights the many physicochemical merits of MTV-MOFs which make them uniquely suited for addressing the shortcomings of sulfur cathodes in practical LSBs.

ASSOCIATED CONTENT

5 Supporting Information

The Supporting Information is available free of charge at https://pubs.acs.org/doi/10.1021/acsami.3c15480.

Experimental and theoretical methods, battery electrochemical measurements; characterization of CoNiFe-MOF-74, CoNiFe₃O₄/PC, and S@CoNiFe₃O₄/PC; and comparison study (PDF)

AUTHOR INFORMATION

Corresponding Author

Hani M. El-Kaderi — Department of Chemistry, Virginia Commonwealth University, Richmond, Virginia 23284, United States; Oorcid.org/0000-0001-8770-1544; Email: helkaderi@vcu.edu; Fax: (804) 828-8599

Authors

Mahmoud M. Kaid — Department of Chemistry, Virginia Commonwealth University, Richmond, Virginia 23284, United States; Department of Chemistry, Faculty of Science, Mansoura University, Mansoura 35516, Egypt; orcid.org/ 0000-0002-9173-0169

Mohammad K. Shehab — Department of Chemistry, Virginia Commonwealth University, Richmond, Virginia 23284, United States; orcid.org/0000-0001-6626-3012

Hong Fang — Department of Physics, Virginia Commonwealth University, Richmond, Virginia 23284, United States; Department of Physics, Rutgers University, Camden, New Jersey 08102, United States; orcid.org/0000-0002-0968-

Awad I. Ahmed – Department of Chemistry, Faculty of Science, Mansoura University, Mansoura 35516, Egypt

Sohier A. El-Hakam – Department of Chemistry, Faculty of Science, Mansoura University, Mansoura 35516, Egypt

Amr Awad Ibrahim — Department of Chemistry, Faculty of Science, Mansoura University, Mansoura 35516, Egypt;
orcid.org/0000-0002-1315-6616

Puru Jena – Department of Physics, Virginia Commonwealth University, Richmond, Virginia 23284, United States; orcid.org/0000-0002-2316-859X

Complete contact information is available at: https://pubs.acs.org/10.1021/acsami.3c15480

Note:

The authors declare no competing financial interest.

ACKNOWLEDGMENTS

Research reported in this publication was supported by the U.S.-Egypt Science and Technology (S&T) Joint Fund with funding provided by the United States Agency for International Development (USAID) through the National Academies of Sciences, Engineering, and Medicine (National Academies) under award number: SCON-10000859. H.M.K. acknowledges the support of the Institute for Sustainable Energy and Environment (ISEE) at Virginia Commonwealth University. M.M.K. gratefully acknowledges the financial support by the Egyptian Ministry of Higher Education and Scientific Research for the Joint Supervision Ph.D. Fellowship. M.K.S. acknowledges Altria fellowship for its support. The authors acknowledge Michael L. Ritch for modifying the synthetic scheme and Alexander J. Richard for helping with XPS data processing. P.J. acknowledges partial support by the U.S. Department of Energy, Office of Basic Energy Sciences, Division of Materials Sciences and Engineering under award no. DE-FG02-96ER45579. Resources of the National Energy Research Scientific Computing (NERSC) Center supported by the Office of Science of the U.S. Department of Energy under contract no. DE-AC02-05CH11231, as well as that of the High-Performance Research Computing (HPRC) core facility at Virginia Commonwealth University, are also acknowledged.

REFERENCES

- (1) Liang, Z.; He, J.; Hu, C.; Pu, X.; Khani, H.; Dai, L.; Fan, D.; Manthiram, A.; Wang, Z.-L. Next-Generation Energy Harvesting and Storage Technologies for Robots Across All Scales. *Adv. Intell. Syst.* **2022**, *5*, 2200045.
- (2) Huang, Y.; Lin, L.; Zhang, C.; Liu, L.; Li, Y.; Qiao, Z.; Lin, J.; Wei, Q.; Wang, L.; Xie, Q.; Peng, D. L. Recent Advances and Strategies toward Polysulfides Shuttle Inhibition for High-Performance Li-S Batteries. *Adv. Sci.* **2022**, *9*, 2106004.
- (3) Deng, S.; Guo, T.; Heier, J.; Zhang, C. Unraveling Polysulfide's Adsorption and Electrocatalytic Conversion on Metal Oxides for Li-S Batteries. *Adv. Sci.* **2023**, *10*, 2204930.
- (4) Wu, J.; Ye, T.; Wang, Y.; Yang, P.; Wang, Q.; Kuang, W.; Chen, X.; Duan, G.; Yu, L.; Jin, Z.; Qin, J.; Lei, Y. Understanding the Catalytic Kinetics of Polysulfide Redox Reactions on Transition Metal Compounds in Li-S Batteries. ACS Nano 2022, 16, 15734–15759.
- (5) Pang, Q.; Liang, X.; Kwok, C. Y.; Nazar, L. F. Advances in Lithium-Sulfur Batteries Based on Multifunctional Cathodes and Electrolytes. *Nat. Energy* **2016**, *1*, 16132.
- (6) Abdelkader, A. A.; Rodene, D. D.; Norouzi, N.; Alzharani, A.; Weeraratne, K. S.; Gupta, R. B.; El-Kaderi, H. M. Multifunctional Electrocatalytic Cathodes Derived from Metal-Organic Frameworks for Advanced Lithium-Sulfur Batteries. *Chem.—Eur. J.* **2020**, *26* (61), 13896–13903.
- (7) Wang, J.; Ding, B.; Lu, X.; Nara, H.; Sugahara, Y.; Yamauchi, Y. Single Atom-Based Nanoarchitectured Electrodes for High-Performance Lithium-Sulfur Batteries. *Adv. Mater. Interfaces* **2021**, *8*, 2002159.
- (8) Hong, X. J.; Song, C. L.; Yang, Y.; Tan, H. C.; Li, G. H.; Cai, Y. P.; Wang, H. Cerium Based Metal-Organic Frameworks as an Efficient Separator Coating Catalyzing the Conversion of Polysulfides for High Performance Lithium-Sulfur Batteries. *ACS Nano* **2019**, *13* (2), 8b08155.
- (9) Fang, R.; Zhao, S.; Sun, Z.; Wang, D. W.; Cheng, H. M.; Li, F. More Reliable Lithium-Sulfur Batteries: Status, Solutions and Prospects. *Adv. Mater.* **2017**, *29*, 1606823.
- (10) Lin, H.; Yang, L.; Jiang, X.; Li, G.; Zhang, T.; Yao, Q.; Zheng, G. W.; Lee, J. Y. Electrocatalysis of Polysulfide Conversion by Sulfur-

- Deficient MoS₂ Nanoflakes for Lithium-Sulfur Batteries. *Energy Environ. Sci.* **2017**, *10* (6), 1476–1486.
- (11) Zhou, G.; Tian, H.; Jin, Y.; Tao, X.; Liu, B.; Zhang, R.; Seh, Z. W.; Zhuo, D.; Liu, Y.; Sun, J.; Zhao, J.; Zu, C.; Wu, D. S.; Zhang, Q.; Cui, Y. Catalytic Oxidation of Li₂S on the Surface of Metal Sulfides for Li-S Batteries. *Proc. Natl. Acad. Sci. U.S.A.* **2017**, *114* (5), 840–845.
- (12) He, J.; Bhargav, A.; Manthiram, A. Molybdenum Boride as an Efficient Catalyst for Polysulfide Redox to Enable High-Energy-Density Lithium-Sulfur Batteries. *Adv. Mater.* **2020**, 32 (40), 2004741.
- (13) Mahankali, K.; Nagarajan, S.; Thangavel, N. K.; Rajendran, S.; Yeddala, M.; Arava, L. M. R. Metal-Based Electrocatalysts for High-Performance Lithium-Sulfur Batteries: A Review. *Catalyst* **2020**, *10* (10), 1137.
- (14) Zhou, X.; Zeng, P.; Yu, H.; Guo, C.; Miao, C.; Guo, X.; Chen, M.; Wang, X. Engineering a TiNb₂O₇-Based Electrocatalyst on a Flexible Self-Supporting Sulfur Cathode for Promoting Li-S Battery Performance. ACS Appl. Mater. Interfaces **2022**, 14 (1), 1157–1168.
- (15) Liang, X.; Hart, C.; Pang, Q.; Garsuch, A.; Weiss, T.; Nazar, L. F. A Highly Efficient Polysulfide Mediator for Lithium-Sulfur Batteries. *Nat. Commun.* **2015**, *6*, 5682.
- (16) Wang, Y.; Zhang, R.; Chen, J.; Wu, H.; Lu, S.; Wang, K.; Li, H.; Harris, C. J.; Xi, K.; Kumar, R. V.; Ding, S. Enhancing Catalytic Activity of Titanium Oxide in Lithium-Sulfur Batteries by Band Engineering. *Adv. Energy Mater.* **2019**, *9* (24), 1900953.
- (17) Gu, L. L.; Wang, C.; Qiu, S. Y.; Wang, K. X.; Gao, X. T.; Zuo, P. J.; Sun, K. N.; Zhu, X. D. Cobalt-Iron Oxide Nanotubes Decorated with Polyaniline as Advanced Cathode Hosts for Li-S Batteries. *Electrochim. Acta* **2021**, *390*, 138873.
- (18) He, Y.; Xu, L.; Li, C.; Chen, X.; Xu, G.; Jiao, X. Mesoporous Mn-Sn Bimetallic Oxide Nanocubes as Long Cycle Life Anodes for Li-Ion Half/Full Cells and Sulfur Hosts for Li-S Batteries. *Nano Res.* **2018**, *11* (7), 3555–3566.
- (19) He, J.; Bhargav, A.; Manthiram, A. High-Performance Anode-Free Li-S Batteries with an Integrated Li₂S-Electrocatalyst Cathode. *ACS Energy Lett.* **2022**, *7* (2), 583–590.
- (20) He, Y.; Li, M.; Zhang, Y.; Shan, Z.; Zhao, Y.; Li, J.; Liu, G.; Liang, C.; Bakenov, Z.; Li, Q. All-Purpose Electrode Design of Flexible Conductive Scaffold toward High-Performance Li-S Batteries. *Adv. Funct. Mater.* **2020**, *30* (19), 2000613.
- (21) Chen, Y.; Zhang, W.; Zhou, D.; Tian, H.; Su, D.; Wang, C.; Stockdale, D.; Kang, F.; Li, B.; Wang, G. Co-Fe Mixed Metal Phosphide Nanocubes with Highly Interconnected-Pore Architecture as an Efficient Polysulfide Mediator for Lithium-Sulfur Batteries. *ACS Nano* **2019**, *13* (4), 4731–4741.
- (22) Shi, Z.; Sun, Z.; Cai, J.; Fan, Z.; Jin, J.; Wang, M.; Sun, J. Boosting Dual-Directional Polysulfide Electrocatalysis via Bimetallic Alloying for Printable Li-S Batteries. *Adv. Funct. Mater.* **2021**, *31* (4), 2006798.
- (23) He, J.; Bhargav, A.; Manthiram, A. High-Energy-Density, Long-Life Lithium-Sulfur Batteries with Practically Necessary Parameters Enabled by Low-Cost Fe-Ni Nanoalloy Catalysts. *ACS Nano* **2021**, *15* (5), 8583–8591.
- (24) Kaid, M. M.; Gebreil, A.; El-Hakam, S. A.; Ahmed, A. I.; Ibrahim, A. A. Sulfamic Acid Incorporated HKUST-1: A Highly Active Catalyst and Efficient Adsorbent. *RSC Adv.* **2020**, *10* (26), 15586–15597.
- (25) Kaid, M. M.; Elbanna, O.; El-Hakam, S. A.; El-Kaderi, H. M.; Ibrahim, A. A. Effective Photocatalytic Degradation of Organic Dyes Using ZNC/RGO Nanocomposite Photocatalyst Derived from ZIF-8/RGO Thermolysis for Water Treatment. *J. Photochem. Photobiol., A* **2022**, *430*, 114001.
- (26) Ibrahim, A. A.; Kaid, M. M.; Ali, S. L.; Samra, S. E.; El-Hakam, S. A.; Ahmed, A. I. Applications of Nanostructure Phosphomolybdic Acid/Strontium MOF for Removal of Rhodamine B and Synthesis of Pharmaceutically Significant 14-Aryl-14-Alkyl-14-H-Dibenzoxanthene and 7-Hydroxy-4-Methyl Coumarin. *Inorg. Chem. Commun.* 2023, 153, 110748.

- (27) Guo, S.; Xu, X.; Liu, J.; Zhang, Q.; Wang, H. In Situ Growth of Ni-Doped Co-MOF-74 on Ni Foam for High-Performance Electrochemical Energy Storage. *J. Electrochem. Soc.* **2020**, *167* (2), 020539.
- (28) Gamal, S.; Kospa, D. A.; Kaid, M. M.; El-Hakam, S. A.; Ahmed, A. I.; Ibrahim, A. A. Fe-Co Spinel Oxides Supported UiO-66-NH2derived Zirconia/N-Dopped Porous Hollow Carbon as an Efficient Oxygen Reduction Reaction Electrocatalyst. *J. Environ. Chem. Eng.* **2023**, *11* (2), 109359.
- (29) Li, G.; Yang, H.; Li, F.; Du, J.; Shi, W.; Cheng, P. Facile Formation of a Nanostructured NiP₂@C Material for Advanced Lithium-Ion Battery Anode Using Adsorption Property of Metal-Organic Framework. *J. Mater. Chem. A* **2016**, 4 (24), 9593–9599.
- (30) Jiang, S.; Li, X. L.; Fang, D.; Lieu, W. Y.; Chen, C.; Khan, M. S.; Li, D. S.; Tian, B.; Shi, Y.; Yang, H. Y. Metal-Organic-Framework-Derived 3D Hierarchical Matrixes for High-Performance Flexible Li-S Batteries. ACS Appl. Mater. Interfaces 2023, 15 (16), 20064–20074.
- (31) Raza, H.; Cheng, J.; Lin, C.; Majumder, S.; Zheng, G.; Chen, G. High-Entropy Stabilized Oxides Derived via a Low-Temperature Template Route for High-Performance Lithium-Sulfur Batteries. *EcoMat* **2023**, *5* (4), No. e12324.
- (32) Tao, X.; Yang, Z.; Yan, R.; Cheng, M.; Ma, T.; Cao, S.; Bai, M.; Ran, F.; Cheng, C.; Yang, W. Engineering MOFs-Derived Nanoarchitectures with Efficient Polysulfides Catalytic Sites for Advanced Li-S Batteries. *Adv. Mater. Technol.* **2023**, *8* (2), 2200238.
- (33) Li, W.; Guo, X.; Geng, P.; Du, M.; Jing, Q.; Chen, X.; Zhang, G.; Li, H.; Xu, Q.; Braunstein, P.; Pang, H. Rational Design and General Synthesis of Multimetallic Metal-Organic Framework Nano-Octahedra for Enhanced Li-S Battery. *Adv. Mater.* **2021**, 33 (45), 2105163.
- (34) Zhang, S.; Yang, Z.; Gong, K.; Xu, B.; Mei, H.; Zhang, H.; Zhang, J.; Kang, Z.; Yan, Y.; Sun, D. Temperature Controlled Diffusion of Hydroxide Ions in 1D Channels of Ni-MOF-74 for Its Complete Conformal Hydrolysis to Hierarchical Ni(OH)₂ Supercapacitor Electrodes. *Nanoscale* **2019**, *11* (19), 9598–9607.
- (35) He, B.; Zhang, Q.; Pan, Z.; Li, L.; Li, C.; Ling, Y.; Wang, Z.; Chen, M.; Wang, Z.; Yao, Y.; Li, Q.; Sun, L.; Wang, J.; Wei, L. Freestanding Metal-Organic Frameworks and Their Derivatives: An Emerging Platform for Electrochemical Energy Storage and Conversion. *Chem. Rev.* 2022, 122 (11), 10087–10125.
- (36) Zhou, G.; Chen, H.; Cui, Y. Formulating Energy Density for Designing Practical Lithium-Sulfur Batteries. *Nat. Energy* **2022**, *7* (4), 312–319.
- (37) Wang, X.; Xiao, H.; Li, A.; Li, Z.; Liu, S.; Zhang, Q.; Gong, Y.; Zheng, L.; Zhu, Y.; Chen, C.; Wang, D.; Peng, Q.; Gu, L.; Han, X.; Li, J.; Li, Y. Constructing NiCo/Fe₃O₄ Heteroparticles within MOF-74 for Efficient Oxygen Evolution Reactions. *J. Am. Chem. Soc.* **2018**, *140* (45), 15336–15341.
- (38) Wang, L. J.; Deng, H.; Furukawa, H.; Gándara, F.; Cordova, K. E.; Peri, D.; Yaghi, O. M. Synthesis and Characterization of Metal-Organic Framework-74 Containing 2, 4, 6, 8, and 10 Different Metals. *Inorg. Chem.* **2014**, 53 (12), 5881–5883.
- (39) Shamsutdinov, G.; Zhao, P.; Bhattiprolu, S.; Zhao, J. C.; Nadgorny, B. Magnetization-Structure-Composition Phase Diagram Mapping in Co-Fe-Ni Alloys Using Diffusion Multiples and Scanning Hall Probe Microscopy. *Sci. Rep.* **2022**, *12* (1), 1957.
- (40) Mukhtar, A.; Shahzad Khan, B.; Mehmood, T. Appropriate Deposition Parameters for Formation of Fcc Co-Ni Alloy Nanowires during Electrochemical Deposition Process. *Appl. Phys. A: Mater. Sci. Process.* **2016**, 122 (12), 1022.
- (41) Liu, P.; Chen, D.; Wang, Q.; Xu, P.; Long, M.; Duan, H. Crystal Structure and Mechanical Properties of Nickel-Cobalt Alloys with Different Compositions: A First-Principles Study. *J. Phys. Chem. Solids* **2020**, *137*, 109194.
- (42) Li, J. Y.; Li, W.; Jin, M. J.; Jin, X. J. Strain-Induced Reverse Phase Transformation in Nanocrystalline Co-Ni Alloys. *Mater. Res. Lett.* **2015**, 3 (2), 107–113.
- (43) Xie, Z.; Wang, Y. Metal-Organic Framework-Derived CoNi-Embedded Carbon Nanocages as Efficient Electrocatalysts for Oxygen Evolution Reaction. *Ionics (Kiel)* **2018**, 24 (6), 1773–1780.

- (44) Loh, K. S.; Lee, Y. H.; Musa, A.; Salmah, A. A.; Zamri, I. Use of Fe₃O₄ Nanoparticles for Enhancement of Biosensor Response to the Herbicide 2,4-Dichlorophenoxyacetic Acid. *Sensors* **2008**, 8 (9), 5775–5791.
- (45) Liang, C.; Huang, S.; Zhao, W.; Liu, W.; Chen, J.; Liu, H.; Tong, Y. Polyhedral Fe₃O₄ Nanoparticles for Lithium Ion Storage. *New J. Chem.* **2015**, 39 (4), 2651–2656.
- (46) Ahn, I. K.; Joo, W.; Lee, J. H.; Kim, H. G.; Lee, S. Y.; Jung, Y.; Kim, J. Y.; Lee, G. B.; Kim, M.; Joo, Y. C. Metal-Organic Framework-Driven Porous Cobalt Disulfide Nanoparticles Fabricated by Gaseous Sulfurization as Bifunctional Electrocatalysts for Overall Water Splitting. *Sci. Rep.* **2019**, *9* (1), 19539.
- (47) Žhang, Y.; Sun, C.; Su, H.; Huang, W.; Dong, X. N-Doped Carbon Coated Hollow Ni_xCo_{9-X}S₈ Urchins for a High Performance Supercapacitor. *Nanoscale* **2015**, 7 (7), 3155–3163.
- (48) Wu, H.; Lu, Q.; Zhang, J.; Wang, J.; Han, X.; Zhao, N.; Hu, W.; Li, J.; Chen, Y.; Deng, Y. Thermal Shock-Activated Spontaneous Growing of Nanosheets for Overall Water Splitting. *Nano-Micro Lett.* **2020**, *12* (1), 162–5261.
- (49) Sui, Y. W.; Zhang, Y. M.; Hou, P. H.; Qi, J. Q.; Wei, F. X.; He, Y. Z.; Meng, Q. K.; Sun, Z. Three-Dimensional NiCo₂S₄ Nanosheets as High-Performance Electrodes Materials for Supercapacitors. *J. Mater. Sci.* **2017**, 52 (12), 7100–7109.
- (50) Gao, S.; Yang, S. H.; Wang, H. Y.; Wang, G. S.; Yin, P. G.; Zhang, X. J. CoNi Alloy with Tunable Magnetism Encapsulated by N-Doped Carbon Nanosheets toward High-Performance Microwave Attenuation. *Composites, Part B* **2021**, *215*, 108781.
- (51) Pathak, S.; Verma, R.; Singhal, S.; Chaturvedi, R.; Kumar, P.; Sharma, P.; Pant, R. P.; Wang, X. Spin Dynamics Investigations of Multifunctional Ambient Scalable Fe₃O₄ Surface Decorated ZnO Magnetic Nanocomposite Using FMR. Sci. Rep. **2021**, 11 (1), 3799.
- (52) Wu, H.; Huang, F.; Wang, B.; Wang, S.; Nie, W.; Li, S.; Liu, F.; Zhang, H. Decorating CoNi Alloy-Encapsulated Carbon Nanotube Hollow Nanocages to Enable Dielectric Loss for Highly Efficient Microwave Absorption. ACS Appl. Nano Mater. 2022, 5 (9), 13187—13197.
- (53) Shit, S.; Chhetri, S.; Jang, W.; Murmu, N. C.; Koo, H.; Samanta, P.; Kuila, T. Cobalt Sulfide/Nickel Sulfide Heterostructure Directly Grown on Nickel Foam: An Efficient and Durable Electrocatalyst for Overall Water Splitting Application. ACS Appl. Mater. Interfaces 2018, 10 (33), 27712–27722.
- (54) Morais, A.; Alves, J. P. C.; Lima, F. A. S.; Lira-Cantu, M.; Nogueira, A. F. Enhanced Photovoltaic Performance of Inverted Hybrid Bulk-Heterojunction Solar Cells Using TiO 2/Reduced Graphene Oxide Films as Electron Transport Layers. *J. Photonics Energy* **2015**, *5* (1), 057408.
- (55) Bagri, A.; Mattevi, C.; Acik, M.; Chabal, Y. J.; Chhowalla, M.; Shenoy, V. B. Structural Evolution during the Reduction of Chemically Derived Graphene Oxide. *Nat. Chem.* **2010**, *2* (7), 581–587.
- (56) Khassin, A. A.; Yurieva, T. M.; Kaichev, V. V.; Bukhtiyarov, V. I.; Budneva, A. A.; Paukshtis, E. A.; Parmon, V. N. Metal-Support Interactions in Cobalt-Aluminum Co-Precipitated Catalysts: XPS and CO Adsorption Studies. *J. Mol. Catal. A: Chem.* **2001**, *175*, 189–204.
- (57) Tarditi, A. M.; Barroso, N.; Galetti, A. E.; Arrúa, L. A.; Cornaglia, L.; Abello, M. C. XPS Study of the Surface Properties and Ni Particle Size Determination of Ni-Supported Catalysts. *Surf. Interface Anal.* **2014**, *46* (8), 521–529.
- (58) Rajan, A.; Sharma, M.; Sahu, N. K. Assessing Magnetic and Inductive Thermal Properties of Various Surfactants Functionalised Fe₃O₄ Nanoparticles for Hyperthermia. *Sci. Rep.* **2020**, *10* (1), 15045.
- (59) Yan, W.; Gao, X.; Yang, J. L.; Xiong, X.; Xia, S.; Huang, W.; Chen, Y.; Fu, L.; Zhu, Y.; Wu, Y. Boosting Polysulfide Catalytic Conversion and Facilitating Li⁺ Transportation by Ion-Selective COFs Composite Nanowire for Li-S Batteries. *Small* **2022**, *18* (11), 2106679.
- (60) Yan, T.; Wu, Y.; Gong, F.; Cheng, C.; Yang, H.; Mao, J.; Dai, K.; Cheng, L.; Cheng, T.; Zhang, L. TiH₂ Nanodots Exfoliated via

- Facile Sonication as Bifunctional Electrocatalysts for Li-S Batteries. ACS Appl. Mater. Interfaces 2022, 14 (5), 6937–6944.
- (61) Zhang, Y.; Peng, Y.; Wang, Y.; Li, J.; Li, H.; Zeng, J.; Wang, J.; Hwang, B. J.; Zhao, J. High Sulfur-Containing Carbon Polysulfide Polymer as a Novel Cathode Material for Lithium-Sulfur Battery. *Sci. Rep.* 2017, 7 (1), 11386.
- (62) Alzharani, A.; Shehab, M. K.; Rodene, D. D.; Ahmed, J. U.; Bakry, A. M.; Kaid, M. M.; El-Kaderi, H. M. Surface Modification of Partially Reduced Graphene Oxide for Advanced Electrode Material in Rechargeable Sodium Batteries. *Energy Fuels* **2022**, *36* (9), 4967–4977.
- (63) Guo, H.; Zhang, X.; He, W.; Yang, X.; Liu, Q.; Li, M.; Wang, J. Fabricating Three-Dimensional Mesoporous Carbon Network-Coated LiFePO₄/Fe Nanospheres Using Thermal Conversion of Alginate-Biomass. *RSC Adv.* **2016**, *6* (21), 16933–16940.
- (64) Abdul Razzaq, A.; Yao, Y.; Shah, R.; Qi, P.; Miao, L.; Chen, M.; Zhao, X.; Peng, Y.; Deng, Z. High-Performance Lithium Sulfur Batteries Enabled by a Synergy between Sulfur and Carbon Nanotubes. *Energy Storage Mater.* **2019**, *16*, 194–202.
- (65) Lin, Z.; Liu, Z.; Fu, W.; Dudney, N. J.; Liang, C. Lithium Polysulfidophosphates: A Family of Lithium-Conducting Sulfur-Rich Compounds for Lithium-Sulfur Batteries. *Angew. Chem., Int. Ed.* **2013**, 52 (29), 7460–7463.
- (66) Zhang, Y.; Kang, C.; Zhao, W.; Song, Y.; Zhu, J.; Huo, H.; Ma, Y.; Du, C.; Zuo, P.; Lou, S.; Yin, G. D-p Hybridization-Induced "Trapping-Coupling-Conversion" Enables High-Efficiency Nb Single-Atom Catalysis for Li-S Batteries. *J. Am. Chem. Soc.* **2023**, *145* (3), 1728–1739.
- (67) Dong, X.; Liu, X.; Shen, P. K.; Zhu, J. Phase Evolution of VC-VO Heterogeneous Particles to Facilitate Sulfur Species Conversion in Li-S Batteries. *Adv. Funct. Mater.* **2023**, 33 (3), 2210987.
- (68) Feng, Y.; Wang, G.; Ju, J.; Zhao, Y.; Kang, W.; Deng, N.; Cheng, B. Towards High Energy Density Li-S Batteries with High Sulfur Loading: From Key Issues to Advanced Strategies. *Energy Storage Mater.* **2020**, *32*, *320*–*355*.
- (69) Senthil, C.; Jung, H. Y. Molecular Polysulfide-Scavenging Sulfurized-Triazine Polymer Enable High Energy Density Li-S Battery under Lean Electrolyte. *Energy Storage Mater.* **2023**, *55*, 225–235.
- (70) Yoshie, Y.; Hori, K.; Mae, T.; Noda, S. High-Energy-Density Li-S Battery with Positive Electrode of Lithium Polysulfides Held by Carbon Nanotube Sponge. *Carbon* **2021**, *182*, 32–41.